MODELLING OF GRANULAR FLOW ON MICRO- AND MACROSCOPIC SCALES WITH CALIBRATION USING EXPERIMENTAL AND NUMERICAL SETUPS

Robert Hesse[1], Dominik Gilberg[2], Konrad Steiner[2] and Sergiy Antonyuk[1]

[1] Institute of Particle Process Engineering, Technische Universität Kaiserslautern
Gottlieb-Daimler-Straße 44, 67663 Kaiserslautern, Germany
robert.hesse@mv.uni-kl.de, mvt.mv.uni-kl.de

[2] Fraunhofer Institute for Industrial Mathematics
Fraunhofer-Platz 1, 67663 Kaiserslautern, Germany
dominik.gilberg@itwm.fraunhofer.de, www.itwm.fraunhofer.de

Keywords Powder Flow, Silo Discharge, DEM, Continuum Modelling, Pressure Gradient

Abstract Discrete models are frequently used in research in the area of granular matter. While they provide detailed insights, powder simulations can suffer from high particle counts and immense computational times. Therefore, a macroscopic model is calibrated by experiments and discrete simulations to investigate powder discharge from a wedge-shaped silo for varying orifice sizes. Additional coupling with air flow inside the silo reveals that a compaction and a subsequent expansion of the particle bed during discharge causes pressure gradient forces at the outlet, influencing the mass flow rate. The magnitude of the pressure gradient is dependent on the filling level and the orifice size.

1 INTRODUCTION

The prevalent importance of hoppers and silos for a wide variety of industrial branches is apparent by the strenuous efforts of many researchers to obtain models for the discharge behaviour of those storage devices [1–4]. The magnitude of the mass flow itself and the difficulties in maintaining a reliable, uniform flow behaviour are of great interest, since those issues can have impactful consequences for the following downstream processes.

Therefore, silo and hopper dimensioning plays a vital role in industrial processes. However, even a correctly designed silo setup might experience complications during discharge like mass flow fluctuations due to air interactions, especially for fine powders. Detailed insights into the dynamics during granular flow processes can be achieved with the Discrete Element Method (DEM) and Computational Fluid Dynamics (CFD) coupling [5, 6]. However, the particle size of powders leads to an immense computational effort for this approach, increasing the need for a macroscopic model that can predict powder flow behaviour for industrial scales. The aim of this work is therefore to calibrate a macroscopic granular model for a powder by experiments and DEM simulations. The powder consists of a sieved fraction $(200\ \mu m \leq d_p \leq 250\ \mu m)$ of FlowLac90 lactose particles (Meggle). The focus is the calibration process itself, as well as the granular-air dynamics during discharge and their impact on the mass flow rate.

Calibration and validation are achieved by experimental compressibility tests, as well as DEM simulations and experiments of shear flow with the open source code LIGGGHTS [7]. Macroscopic simulation is achieved with a modified model according to Latz and Schmidt [8]

using the simulation tool GRAIN, which is developed by the Fraunhofer Institute for Industrial Mathematics in Kaiserslautern.

2 METHODS

2.1 Discrete Granular Modelling

The discrete particle modelling is achieved by the DEM. Within the DEM framework, firstly introduced by Cundall and Strack [9], particle trajectories are calculated based on their interactions with contact partners and other applied forces. Contact forces $\vec{F}_c$ are calculated by contact models, which consider material and surface specific parameters like the Young's modulus, particle friction coefficients and surface energy [10–12]. The sum of all forces for particle i with collision partners j and other applied forces allows the calculation of translational velocities $\vec{v}_p$, rotational velocities $\vec{\omega}_p$ and thereby the position and orientation via numerical integration [9, 13].

$$m_{p,i}\frac{d\vec{v}_{p,i}}{dt} = \sum_{j=1}^{J}\vec{F}_{c,ij} + \vec{F}_{g,i} + \sum_{k=1}^{K}\vec{F}_{fluid,i,k} \qquad (1)$$

$$J_{p,i}\frac{d\vec{\omega}_{p,i}}{dt} = \sum_{j=1}^{J}\left(\vec{M}_{t,ij} + \vec{M}_{r,ij}\right)$$

Whereby t, m_p and $\vec{F}_g$ are the time, particle mass and the gravitational force respectively. The sum of all fluid forces $\vec{F}_{fluid}$ includes interaction between particles and the surrounding fluid, like drag or lift. Analogous to the translational equation, the rotational movement includes the moment of inertia J_p and the sum of all torques resulting from tangential contact forces ($\vec{M}_t$) and rolling friction ($\vec{M}_r$). The contact forces are calculated by a combination of Hertz's theory [10] for the elastic normal force component and a modified no-slip condition model of Mindlin [14] proposed by Di Renzo and Di Maio [15] for the tangential force component. Energy dissipation is modelled with the model of Tsuji et al. [16] by adding a viscous damping term, which is related to the coefficient of restitution e. Tangential forces are limited by Coulomb friction. Attractive contact forces due to cohesion are calculated with a simple linear model, which consists of the overlapping contact area between two contact partners multiplied with the cohesion parameter k_{coh} [7, 12].

For this work, the needed parameters for the DEM are the Young's modulus E which was measured by nanoindentation with a flat-punch (TI Premier, Hysitron), the coefficient of restitution e which was obtained analogous to our previous work with a free fall apparatus [17], and the friction coefficient μ_{DEM} and cohesion parameter k_{coh} which both were obtained by calibration with shear tests using a Powder Flow Tester (PFT, Brookfield). While those parameters are essential for the macroscopic calibration process, their detailed measurements processes are beyond the scope of this work.

2.2 Macroscopic Granular Modelling

The macroscopic model is based on a modified approach of Latz and Schmidt [8], whereby granular flow can be modelled in two regimes, namely dense and dilute systems. The spatial resolution is large in contrast to particle sizes. Similar to fluid flow simulations, conservation equations for mass and momentum are solved numerically [8, 18, 19].

$$\frac{\partial}{\partial t}c + \nabla \cdot (c\vec{v}) = 0 \tag{2}$$

$$\frac{\partial}{\partial t}(c\vec{v}) + \nabla \cdot (c\vec{v}\vec{v}^T) = \nabla \cdot (\eta \nabla \vec{v}) - \nabla p + c\vec{g} + \beta\left(\vec{v} - \vec{v}_f\right)$$

Additionally, the conservation of granular temperature which represents the spatial average of the fluctuating granular velocity is coupled with the previous set of equations [20].

$$\frac{\partial}{\partial t}(cT) + \nabla \cdot (cT\vec{v}) = \frac{3}{2}[\eta \nabla \vec{v} : \nabla \vec{v} - \nabla \cdot (\lambda \nabla T)] - \varepsilon_r cT \tag{3}$$

Whereby c, $\vec{v}$, η, p, $\vec{g}$, T, λ and ε_r are the particle volume fraction, granular velocity vector, shear viscosity, granular pressure, gravity vector, granular temperature, thermal conductivity, and the energy dissipation rate, respectively. β represents the momentum exchange term with the velocity differences between the granular and the fluid phases. To solve the conservation equations, several closure relations are needed, which contain parameters which are dependent on the granular material and its compressibility [8, 18, 19].

$$\begin{aligned} g_c &= (1 - c/c_{max})^{-1} & p &= p_k + p_y \\ p_k &= cTg_c & p_y &= \Theta(c - c_0)T_0(c - c_0)g_c \\ \eta &= \eta_0 \cdot \sqrt{T} g_c c \cdot (1 + p_y/p_k) & \lambda &= \lambda_0 \cdot \sqrt{T} g_c c \cdot (1 + p_y/p_k) \\ \varepsilon_r &= \varepsilon_0 \cdot \sqrt{T} g_c \cdot (1 + p_y/p_k) \end{aligned} \tag{4}$$

Whereby g_c is the radial distribution function, which approaches infinity if the granular volume fraction is close to the maximum volume fraction c_{max}. The function g_c implies the frequency for binary collisions in dilute regimes and represents long-term contacts for dense systems. The granular pressure consists of the kinetic part p_k and the yield-pressure p_y. The yield pressure is set to zero with the Heaviside step function, until the minimum yield volume fraction c_0 is reached. The yield pressure has a similar formulation as the kinetic granular pressure, however it uses T_0 as the constant yield parameter which prevents the overall pressure to approach zero for vanishing granular temperature. The shear viscosity, thermal conductivity and energy dissipation rate increase with the ratio of yield to kinetic pressure and depend on the material specific parameters η_0, λ_0, ε_0 respectively. In addition to the equations above, the proposed relation for the bulk friction angle φ, η_0 and ε_0 by Latz and Schmidt is used [8].

$$\tan(\varphi) = \sqrt{\eta_0 \varepsilon_0} \tag{5}$$

Granular-air interaction is accounted for by solving the Navier-Stokes equations for mass and momentum for air. The momentum exchange term β is approximated by the Ergun relation [21]. Additionally, a fluid pressure gradient term is added in the granular momentum equation (Eq. 2).

3 CALIBRATION OF THE MACROSCOPIC MODEL

The procedure for the determination of the material specific parameters described in section 2.2 can be split in two parts. The analysis of the compressibility behaviour, which yields c_0, c_{max} and T_0 was done separately from the remaining unknowns. Afterwards, η_0, ε_0 and λ_0 are obtained by experimental and numerical shear tests.

3.1 Compressibility analysis

The bulk density of the sieved fraction of lactose powder $(200\ \mu m \leq d_p \leq 250\ \mu m)$ was obtained with a standard PFT procedure. The granular volume fraction can be calculated with the particle density value of approximately $\rho_p = 1060 \frac{kg}{m^3}$. With the relations for g_c and p_y (Eq. 4) and the absence of kinetic pressure due to quasi-static compression inside the shear cell, a simple iterative solver can fit for c_0, c_{max} and T_0 by minimizing the sum of the squared error between the experimental and modelled stresses (Fig. 1).

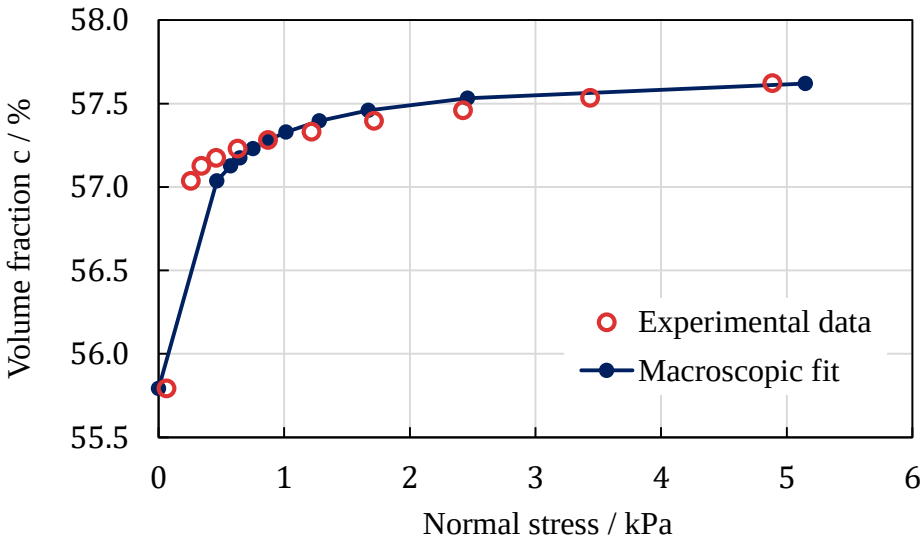

Figure 1: Compressibility measurements and macroscopic fitting with Eq. 4

The fit reaches a good agreement with experimental results. However, for very low stresses, the macroscopic model is slightly less sensitive to pressure changes. The final parameters for c_0, c_{max} and T_0 are shown in Table 1.

Table 1: Macroscopic parameters obtained by compression tests (1/2)

c_0 / −	c_{max} / −	T_0 / $\left(\frac{m}{s}\right)^2$
0.5579	0.5771	0.41

3.2 Shear tests

The next step for further calibration is to utilize shear tests similar to other works [19, 22, 23]. The relation between the friction angle φ, η_0 and ε_0 (Eq. 5) allows for further parametrisation of the granular system. Due to the particle size, cohesion can be neglected with relatively low impact on the overall fitting quality. Therefore, the friction angle is approximated by the stationary shear stress τ divided by the normal stress σ during pre-shearing with the PFT, with $\tan(\varphi) \approx \tau/\sigma$. This procedure is also used for the DEM and macroscopic shear tests in the following sections. The shear procedures were repeated three times for each normal stress, whereby the deviations were below 1 %. Table 2 summarizes the averaged results.

Table 2: Experimental shear tests results for the stress dependent friction angle

σ / kPa	τ / kPa	φ / °
0.208	0.11	27.9
0.384	0.198	27.3
0.718	0.359	26.6
1.349	0.667	26.3
2.553	1.251	26.1
4.845	2.368	26.0

For the wall boundaries (aluminium), a measured constant wall friction angle of $\varphi_x \approx 16°$ is applied. The measured friction angles only give valid ratios and therefore infinite possibilities for the values of η_0 and ε_0 with Eq. 5. For further parameterisation, the next step is to obtain similar velocity profiles in a shear cell with the macroscopic model compared to DEM simulations. For the DEM model, the particle size was set randomly via a Gaussian distribution with an arithmetic mean of $200\,\mu m$. During the particle generation process, particles with diameters below $200\,\mu m$ or above $250\,\mu m$ were iterated again until a size between the sieved fraction was obtained. This approach allowed for a very similar size distribution to the experiments. The measured and calibrated material parameters for the DEM simulations are shown in Table 3.

Table 3: DEM parameters

E / GPa	v / $-$	e / $-$	ρ_p / $\frac{kg}{m^3}$	μ_{DEM} / $-$	k_{coh} / $\frac{J}{m^3}$	d_p / μm
2.5	0.3	0.67	1060	0.95	10^5	$200 - 250$

The shear cell for the DEM and the shear cell for the macroscopic model are an approximate replication of the PFT shear cell and its dimensions (6″ cell) with a purely translational movement. To reduce computation time, the horizontal axes are periodic in both cases, while the macroscopic shear cell model was also kept completely two-dimensional. The setups' dimensions are approximately (length × depth × height) $11\,mm \times 2\,mm \times 20\,mm$.

Shearing was induced by moving fins at the bottom for the DEM, and with a constant boundary velocity for the macroscopic model. For the DEM, the lid was moving vertically to adjust the applied pressure, while no horizontal movement was allowed. Shear velocities were increased to $2\,mm/s$ instead of approximately $0.5\,mm/s$ inside the PFT to reach steady state faster and therefore to further reduce computation time for the DEM. The macroscopic model cell's height was adjusted to only include the particle bed between the upper lid fins and the lower cell fins. It was also adjusted accordingly to the position of the DEM lid, which was dependent on the applied normal stress. Fig. 2 showcases the used shear cell setups exemplarily with $4.845\,kPa$ normal stress applied to the upper shear plane (right below the lid fins) alongside with the horizontal velocity profiles according to the final fitting.

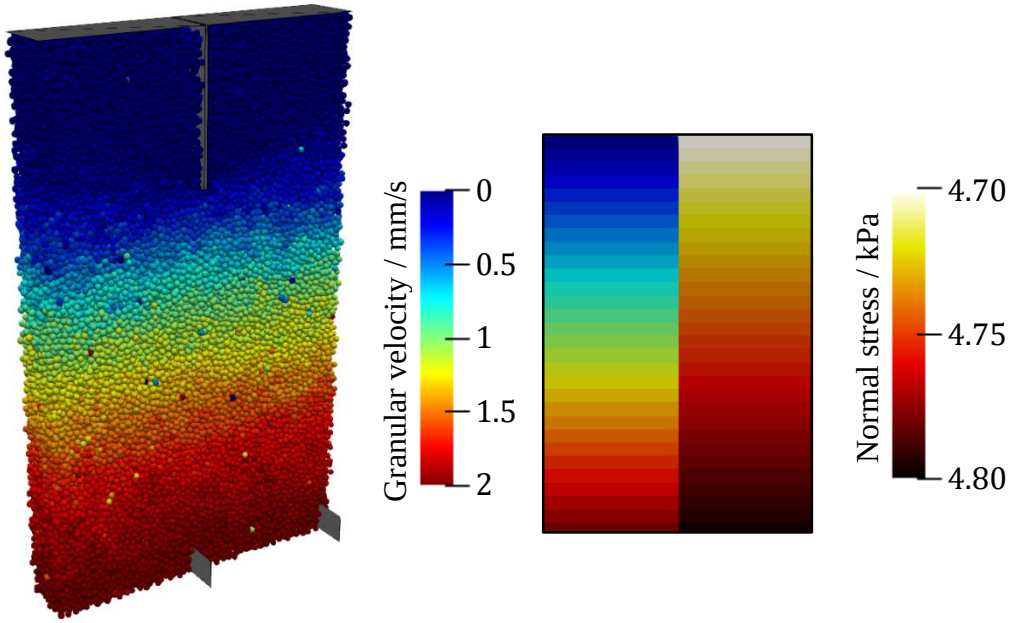

Figure 2: Numerical shear cell setups for DEM (left) and the macroscopic model (right)

An analysis of the horizontal velocity profiles for the same stresses as in Table 2 revealed that the velocities are slightly concave for very low stresses and become more linear with higher stresses. The fitting procedure was started for the lowest stress, for which the concave profile was the most pronounced. Fig. 3 shows the end result of the fitting process with the corresponding normalized velocities for three stresses, whereby the horizontal black lines represent the upper and lower fins of the lid and cell if the lid is resting on the particle bed without compaction.

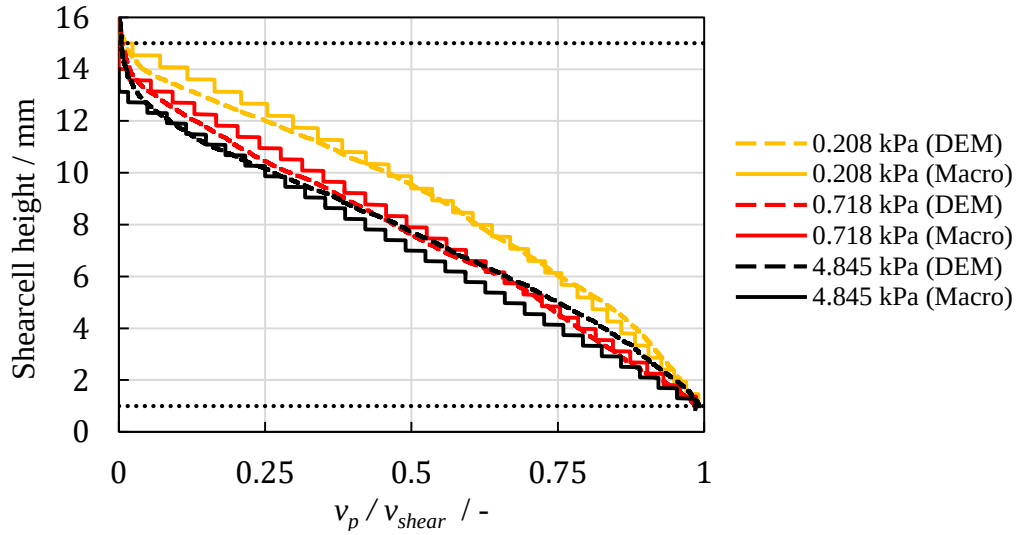

Figure 3: Velocity profiles inside the DEM and macroscopic shear cells for different normal stresses

Fig. 3 shows good agreement between the macroscopic model and the DEM. However, the velocity profile could be adjusted by ratios of η_0 and λ_0, yielding infinite combinations, similar

to Eq. 5. The velocity profiles in Fig. 3 could be achieved with the relation of $\lambda_0 \cdot \eta_0 = 5.2 \cdot 10^{-7}\ m^2$. Therefore, with the shear measurements and Eq. 5, one unknown still remains. Since the shear viscosity heavily influences the outflow time for silo discharge while λ_0 and ε_0 show less influence, η_0 was guessed and iteratively fitted to yield the best outflow time agreement with experimental results, whereby λ_0 and ε_0 could be recalculated easily with the derived relations. More details about the silo setup are shown in the next chapter. The final values of the remaining parameters are depicted in Table 4.

Table 4: Macroscopic parameters obtained by shear tests (2/2)

$\eta_0\ /\ m$	$\lambda_0\ /\ m$	$\varepsilon_0\ /\ m^{-1}$
0.00052	0.001	332.84

Additionally, the ratio of normal to shear stresses were compared to the experimental data in Table 2. It was found that instead of using a stress dependent friction angle according to Table 2 for Eq. 5, a static friction angle of $\varphi = 27°$ led to a better fit, which is summarized in Fig. 4.

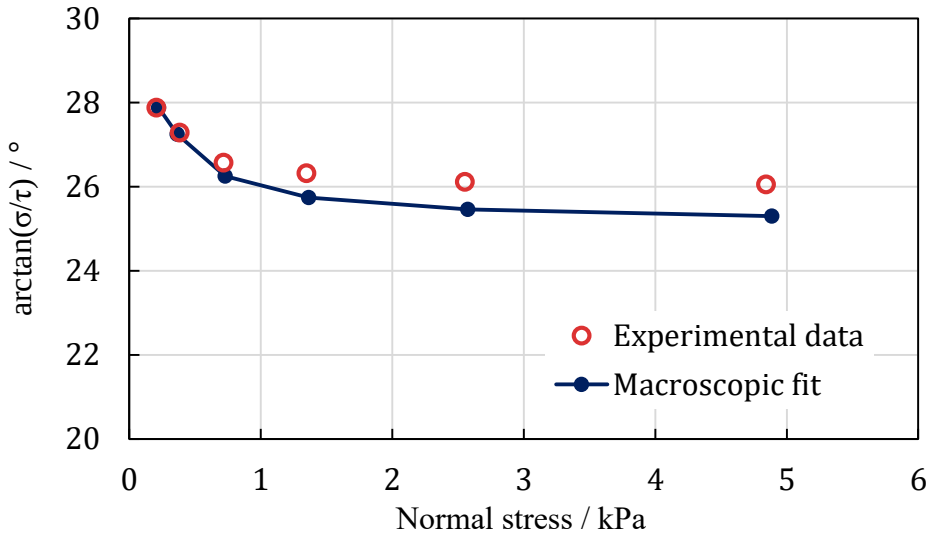

Figure 4: Comparison of the stress dependent friction angle for the macroscopic model

Especially for low stresses, the friction angles show good accordance with the experiments. This is important, since the following silo setup has a filling height below 300 mm, which also yields low normal stresses.

4 SILO DISCHARGE ANALYSIS

The macroscopic model is now applied to silo discharge from a lab scale silo with aluminium walls and adjustable orifice size and hopper half angle. The silo shaft is 200 mm in height, 45 mm in width and 60 mm in depth. Depending on the orifice size and hopper half angle, the hopper has a maximum vertical height of ca. 100 mm. In this work, the half hopper angle θ is fixed at 15°, while the orifice size b is varied between 5 mm, 10 mm and 15 mm.

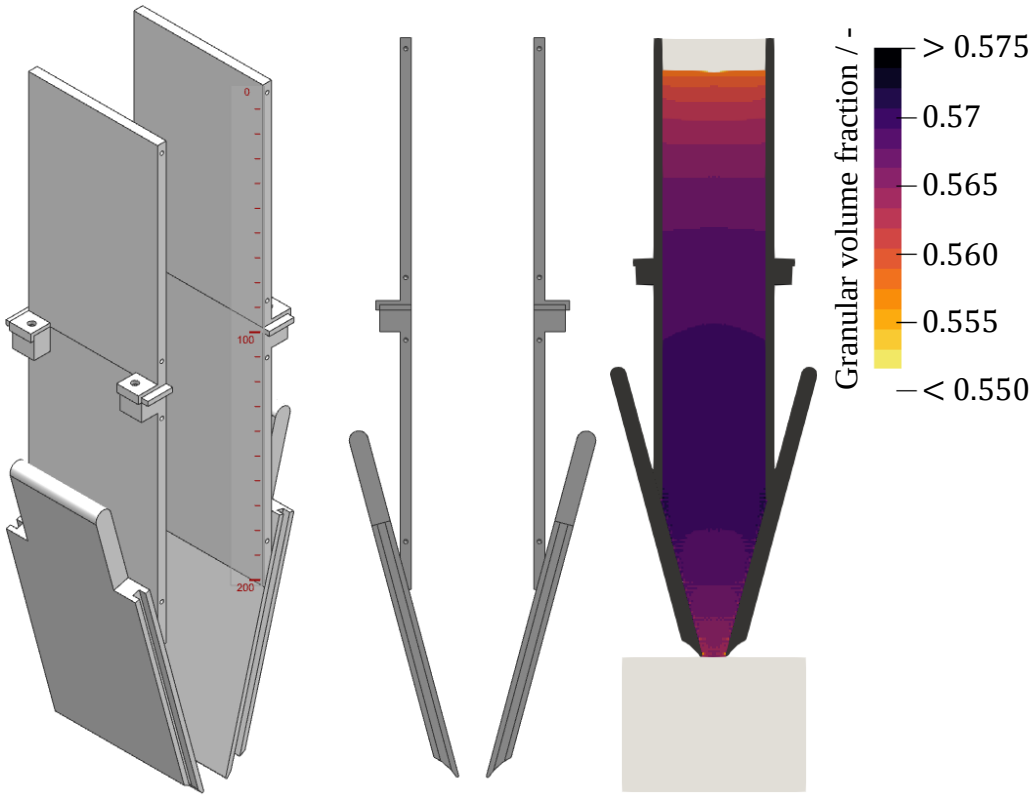

Figure 5: Experimental silo setup for discharge tests (left, middle) and macroscopic representation with the granular volume fraction inside the silo after filling (right)

For the experimental procedure, a 3D printed discharge shutter was held with two electromagnets during filling. Discharge was induced by shutting down the magnets' power supply. The mass flow rate was measured indirectly by weighing the remaining mass inside the silo with an EC 3000-3-FS-AVC (WIPOTEC) high speed scale. For the macroscopic modelling, areas with no granular volume were added on the top and bottom of the silo boundary (see Fig. 5) to allow for better fluid interaction and numerical stability. Similar to the macroscopic shear cell, the silo was two-dimensional and additionally split by a boundary with symmetric conditions in the middle.

4.1 Mass flow rates

For the three different orifice sizes, the mass flow rates depicted in Fig. 6 were obtained. Experiments were repeated three times, whereby only insignificant differences between different runs could be found.

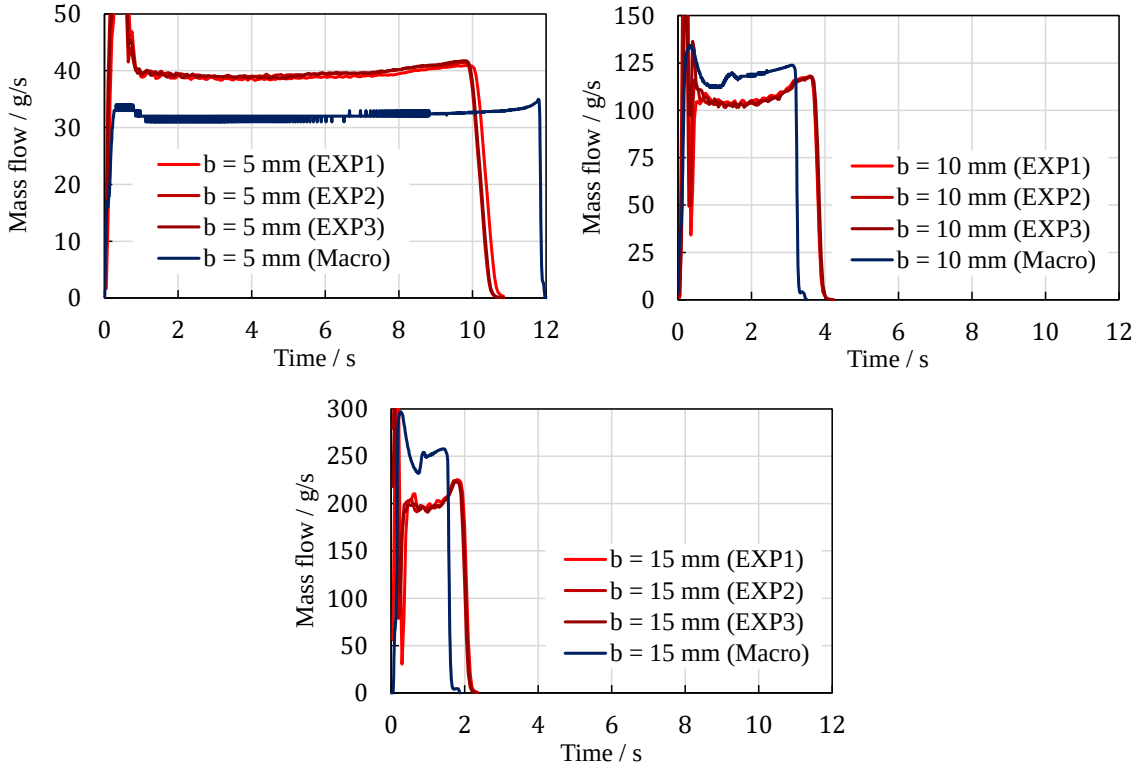

Figure 6: Experimental and numerical mass flow rates

The initial spikes for the experimental mass flows are caused by the shutter drop off. Qualitatively, the changes in mass flow rate over time show a good agreement between simulations and experiments. However, for $b = 5\ mm$, the numerical flow rate is lower than experiments and vice versa for bigger orifices. This might be related to the simple wall friction angle modelling, which has more impact for small openings. After $1\ s$ of outflow time, mass flow decreases and shows a positive trend afterwards. Also, wider orifice sizes cause more rapid mass flow changes.

4.2 Porosity and fluid pressure dynamics

The mass flow profiles in the previous subchapter can be explained by granular-air interaction inside of the silo [24–26]. During discharge, the powder is compacted while nearing the hopper by the decreasing horizontal cross-sectional area. At the orifice however, stress is tending to zero, whereby the bulk expands. These compaction and expansion dynamics lead to a partial vacuum inside of the silo and therefore pressure gradient forces at the outlet, inhibiting bulk acceleration. Fig. 7 emphasizes this for an orifice of $b = 10\ mm$ at varying outflow times.

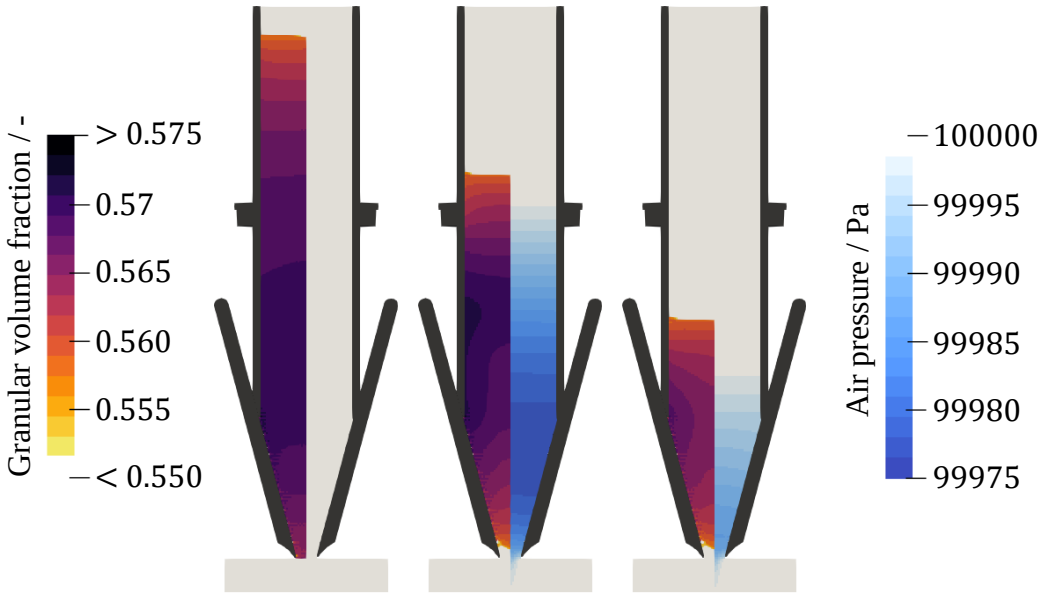

Figure 7: Volume fraction and fluid pressure before discharge (left) and after 1 s and 2 s for $b = 10\ mm$

The rise of mass flow with lower filling levels is caused by less granular pressure and therefore less compaction at the start of the hopper, leading to decreasing air pressure gradients at the outlet. Additionally, less resistance due to the decrease of bed height allows for easier vacuum compensation by air flow from above the silo. Fig. 8 summarizes the pressure gradients for all orifice sizes during the discharge processes.

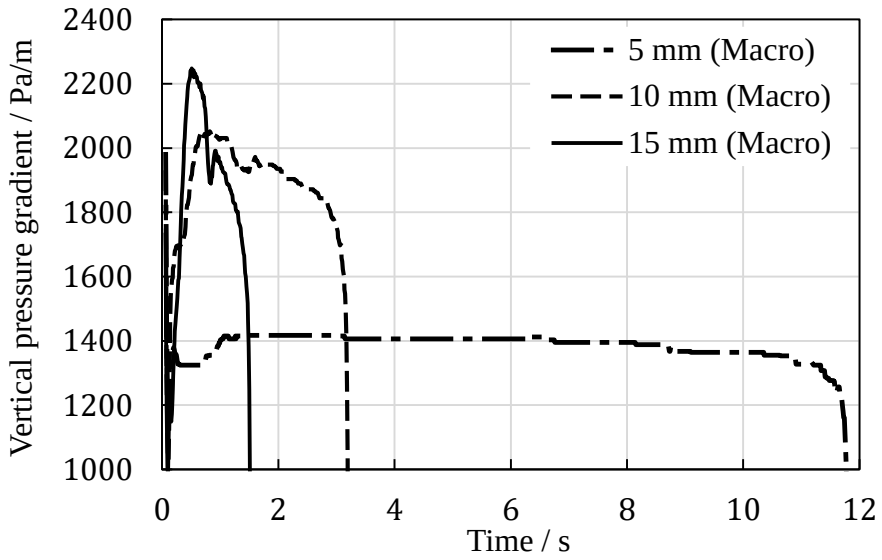

Figure 8: Pressure gradient at the outlet for the studied orifice sizes

Analogous to the mass flow rates, after 1 s of discharge the pressure gradient seems to stabilize and decrease over time. The magnitude and the decrease of the pressure gradients are amplified for bigger orifices.

5 SUMMARY AND OUTLOOK

To counter the numerical difficulties regarding time and computational power for powder modelling with discrete particles, a macroscopic approach was able to capture the characteristics of powder flow adequately. DEM was only used as an additional calibration tool, if experimental setups are unable to provide all necessary data, reducing the overall computational effort significantly. Still, the calibration process is cumbersome and in this case needed information from the investigated process of silo discharge itself. This work also shows the importance of air interaction when considering powder flow modelling. Due to the compressibility of powders, the compaction and expansion dynamics inside silos can have a strong impact on the overall flow behaviour. This can only be accounted for by coupling the granular model with simultaneous fluid calculations.

In the future, additional calibration setups will be used that are more dynamic in contrast to the dense and slow flows in shear cells. The current ongoing step is to utilize a custom powder rheometer setup which also can be modelled with DEM and within the macroscopic model framework GRAIN.

6 ACKNOWLEDGEMENTS

This study is conducted in the framework of the “PowderReg” project, funded by the European programme Interreg VA GR within the priority axis 4 "Strengthen the competitiveness and the attractiveness of the Grande Région / Großregion". Further gratitude goes to WIPOTEC for their support with regards to the measurement equipment.

REFERENCES

[1] Tomas, J. (1991). Modelling of instationary discharge behaviour of cohesive particulate solids out of bunkers. *Chemie-Technik* 43(8), 307–309.

[2] Barletta, D., Donsì, G., Ferrari, G., Poletto, M., Russo, P. (2007). Solid flow rate prediction in silo discharge of aerated cohesive powders. *AIChE J.* 53(9), 2240–2253.

[3] Baserinia, R., Sinka, I.C. (2018). Mass flow rate of fine and cohesive powders under differential air pressure. *Powder Technology* 334, 173–182.

[4] Beverloo, W.A., Leniger, H.A., van de Velde, J. (1961). The flow of granular solids through orifices. *Chemical Engineering Science* 15(3-4), 260–269.

[5] Deen, N.G., van Sint Annaland, M., van der Hoef, M.A., Kuipers, J.A.M. (2007). Review of discrete particle modeling of fluidized beds. *Chemical Engineering Science* 62(1-2), 28–44.

[6] Breuninger, P., Weis, D., Behrendt, I., Grohn, P., Krull, F., Antonyuk, S. (2019). CFD–DEM simulation of fine particles in a spouted bed apparatus with a Wurster tube. *Particuology* 42, 114–125.

[7] Kloss, C., Goniva, C., Hager, A., Amberger, S., Pirker, S. (2012). Models, algorithms and validation for opensource DEM and CFD-DEM. *PCFD* 12(2/3), 140.

[8] Latz, A., Schmidt, S. (2010). Hydrodynamic modeling of dilute and dense granular flow. *Granular Matter* 12(4), 387–397.

[9] Cundall, P.A., Strack, O.D.L. (1979). A discrete numerical model for granular assemblies. *Géotechnique* 29(1), 47–65.

[10] Hertz, H. (1881). Über die Berührung fester elastischer Körper. *Journal für die reine und angewandte Mathematik* (92), 156–171.

[11] Mindlin, R.D., Deresiewicz, H. (1953). Elastic Spheres in Contact under Varying Oblique Force. *Journal of Applied Mechanics* (20), 327–344.

[12] Johnson, K.L., Kendall, K., Roberts, A.D. (1971). Surface Energy and the Contact of Elastic Solids. *Proceedings of the Royal Society A: Mathematical, Physical and Engineering Sciences* 324(1558), 301–313.

[13] Zhu, H.P., Zhou, Z.Y., Yang, R.Y., Yu, A.B. (2007). Discrete particle simulation of particulate systems: Theoretical developments. *Chemical Engineering Science* 62(13), 3378–3396.

[14] Mindlin, R.D. (1949). Compliance of elastic bodies in contact. *Journal of Applied Mechanics* 16, 259–268.

[15] Di Renzo, A., Di Maio, F.P. (2005). An improved integral non-linear model for the contact of particles in distinct element simulations. *Chemical Engineering Science* 60(5), 1303–1312.

[16] Tsuji, Y., Tanaka, T., Ishida, T. (1992). Lagrangian numerical simulation of plug flow of cohesionless particles in a horizontal pipe. *Powder Technology* 71(3), 239–250.

[17] Krull, F., Hesse, R., Breuninger, P., Antonyuk, S. (2018). Impact behaviour of microparticles with microstructured surfaces: Experimental study and DEM simulation. *Chemical Engineering Research and Design* 135, 175–184.

[18] Niedziela, D., Rau, S., Steiner, K., Vita, S. de, Lutsche, M., Richter, M., Schmidt, M., Stoltz, C. (2017). Virtual Characterization of Dense Granular Flow through a Vertically Rotating Feeding Experiment. *Chem. Eng. Technol.* 40(9), 1599–1604.

[19] Bocquet, L., Losert, W., Schalk, D., Lubensky, T.C., Gollub, J.P. (2002). Granular shear flow dynamics and forces: experiment and continuum theory. *Physical review. E, Statistical, nonlinear, and soft matter physics* 65(1 Pt 1), 11307.

[20] Brilliantov, N., Pöschel, T., *Kinetic theory of granular gases*. Oxford, New York: Oxford University Press2004.

[21] Ergun, S. (1952). Fluid Flow through Packed Columns. *Journal of Chemical Engineering Progress* 48(2), 89–94.

[22] GDR MiDi (2004). On dense granular flows. *The European physical journal. E, Soft matter* 14(4), 341–365.

[23] Feise, H.J., Daiß A. (2003). Building a numerical model for bulk materials from standard shear test data. *Task Quarterly* 7(4), 539–547.

[24] Crewdson, B.J., Ormond, A.L., Nedderman, R.M. (1977). Air-impeded discharge of fine particles from a hopper. *Powder Technology* 16(2), 197–207.

[25] Gu, Z.H. (1991). Gravity Flowrate of Bulk Solids from Mass Flow Bins. *Dept. Mechanical Engineering, University of Wollongong* PhD thesis.

[26] Nedderman, R.M., Tüzün, U., Savage, S.B., Houlsby, G.T. (1982). The flow of granular materials—I. *Chemical Engineering Science* 37(11), 1597–1609.